Cell Reports
Physical Science

CellPress
OPEN ACCESS

Article

Repurposing lignin to generate functional afterglow paper

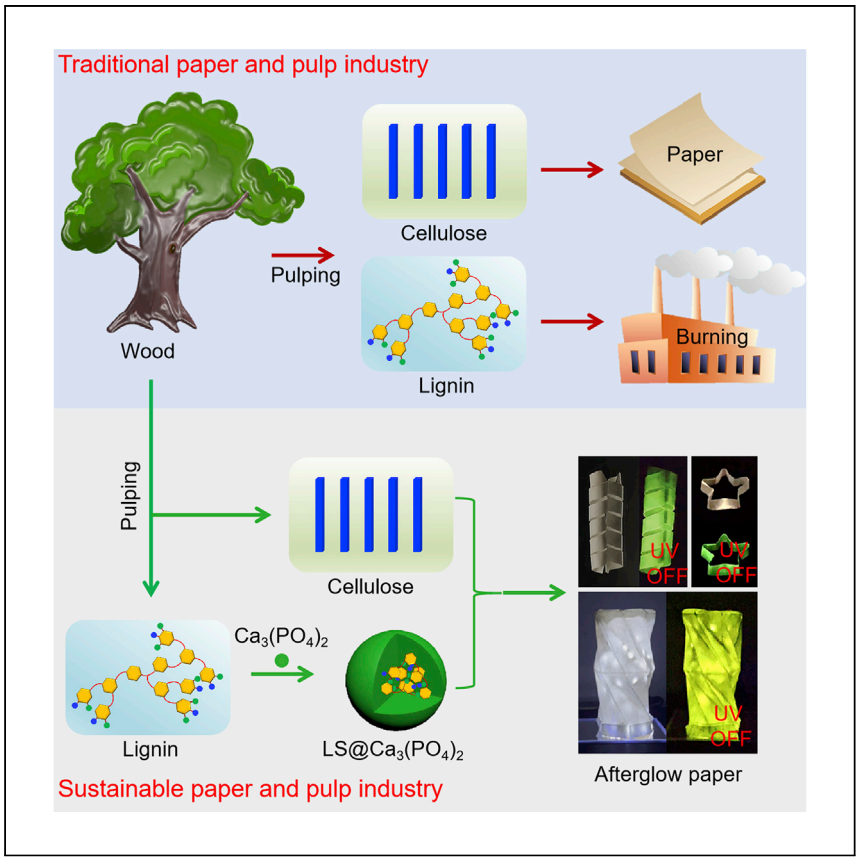

Lignin is a byproduct from the pulp and paper industry, but the utilization of lignin on a large scale remains a significant challenge. Here, Yang et al. report on afterglow additives generating functional paper through the *in situ* confinement of lignin in $Ca_3(PO_4)_2$.

Mingming Yang, Hailong Li, Jing Shen, ..., Zhijun Chen, Meng Li, Tony D. James

chenzhijun@nefu.edu.cn (Z.C.)
mlincepu@hotmail.com (M.L.)
t.d.james@bath.ac.uk (T.D.J.)

Highlights

The syringyl units of lignin sulfonate (LS) generate phosphorescence emission

Afterglow emission of lignin is achieved by combining LS with $Ca_3(PO_4)_2$ ($LS@Ca_3(PO_4)_2$)

Afterglow paper is generated *in situ* from pulp by the generation of $LS@Ca_3(PO_4)_2$

Yang et al., Cell Reports Physical Science 3, 100867
May 18, 2022 © 2022 The Authors.
https://doi.org/10.1016/j.xcrp.2022.100867

Cell Reports
Physical Science

CellPress
OPEN ACCESS

Article

Repurposing lignin to generate functional afterglow paper

Mingming Yang,[1,6] Hailong Li,[4,6] Jing Shen,[1] Shujun Li,[1] Shouxin Liu,[1] Jian Li,[1] Zhijun Chen,[1,7,*] Meng Li,[2,*] and Tony D. James[3,5,*]

SUMMARY

Lignin is a significant byproduct from the pulp and paper industry. However, the conversion of lignin to a resource with added value is plagued by expensive processing. Here we report that the syringyl units (S) of sodium lignosulfonate (LS) exhibit phosphorescence in water with a lifetime of ~2 ms and the lifetime can be prolonged up to ~618 ms by encapsulation in $Ca_3(PO_4)_2$ due to the formation of H-type dimers of the S units (LS@$Ca_3(PO_4)_2$). Motivated by this, we develop afterglow paper through the *in situ* generation of LS@$Ca_3(PO_4)_2$ in the paper matrix. The afterglow emission of the paper is sensitive to H_2O_2, enabling its application as a sensor for liquid/vapor H_2O_2. Moreover, the afterglow paper is shown to be suitable for use in anti-counterfeiting applications, enabling the development of a more sustainable pulp and paper industry.

INTRODUCTION

The pulp and paper industry is essential to the smooth running of society. Annual paper and paperboard production is expected to grow to 900 Mt in 2050.[1] Generally, in the pulp and paper industry, wood is converted to paper pulp and then, processed into paper.[2] Notably, technical lignin is produced as a byproduct in very large quantities (~60–70 Mt per year) during the process.[3,4] Approximately 95% of the as-produced technical lignin is then burned to generate thermal energy in the industry.[3] Among all these technical lignin, lignin sulfonate (LS), accounts for 90% of the as-produced technical lignin. LS is obtained by the addition of NaOH and Na_2S to pulp solution facilitating lignin fractionation from lignocellulose in the paper and pulp industry.[5] Significantly, LS exhibits good water solubility.[6]

From a chemical perspective, lignin, in the wood cell walls, consists of p-hydroxyphenyl (H), guaiacyl (G), and syringyl (S) units, linked by β-O-4 and C-C bonds.[7–9] This chemical structure endows lignin with great potential as a core component for functional materials and aromatic compounds.[10–12] Significantly, the valorization of lignin provides numerous benefits, including extending the life cycle of the carbon contained in lignin and positively contributing to CO_2 neutralization[13,14] Moreover, producing valuable materials/compounds from lignin, rather than simply burning it, can enhance the sustainability of our society.[15] Nevertheless, converting lignin to valuable materials/compounds has experienced problems due to the complicated/variable structure of lignin coupled with the expensive processing required. As such, the most efficient way to use lignin is to directly convert it into functional additives for direct use by the pulp and paper industry, which is vital since such utilization avoids extra treatment steps and additional transportation. Our group and others have shown that the aromatic structures contained within lignin can generate

[1]Engineering Research Center of Advanced Wooden Materials (Northeast Forestry University), Ministry of Education, Harbin 150040, P. R. China

[2]Hebei Key Lab of Power Plant Flue Gas Multi-Pollutants Control, Department of Environmental Science and Engineering, North China Electric Power University, Baoding 071003, P. R. China

[3]Department of Chemistry, University of Bath, Bath BA2 7AY, UK

[4]Department of Physics at Interfaces, Max Planck Institute for Polymer Research, 55128 Mainz, Germany

[5]School of Chemistry and Chemical Engineering, Henan Normal University, Xinxiang 453007, China

[6]These authors contributed equally

[7]Lead contact

*Correspondence:
chenzhijun@nefu.edu.cn (Z.C.),
mlincepu@hotmail.com (M.L.),
t.d.james@bath.ac.uk (T.D.J.)

https://doi.org/10.1016/j.xcrp.2022.100867

This is an open access article under the CC BY license (http://creativecommons.org/licenses/by/4.0/).

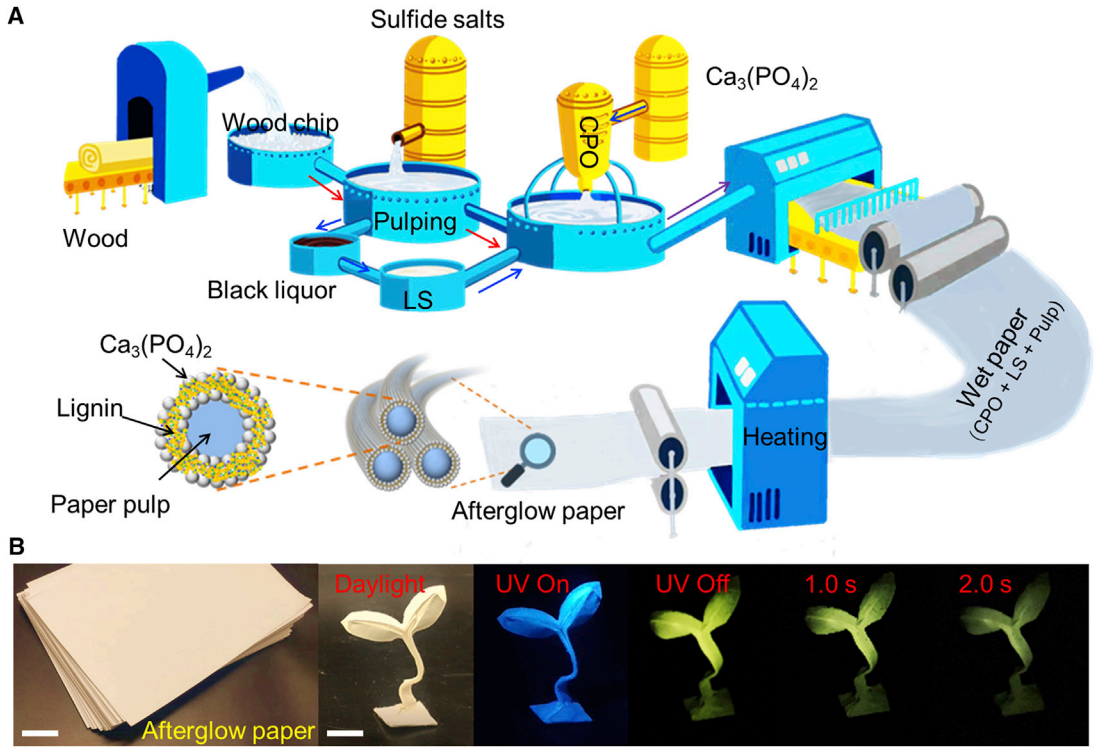

Figure 1. Preparation of afterglow paper using LS

(A) Schematic illustrating the conversion of LS produced as a byproduct in the pulping and paper industry to LS@$Ca_3(PO_4)_2$ for the production of afterglow paper.

(B) Digital image of the afterglow paper and afterglow emission of the folded afterglow paper. Scale bar, 2 cm.

interesting optical and luminescent properties.[16–23] As such, we recognized that we could combine the luminescent properties of lignin during the production of paper *in situ* to develop sensing,[24] packaging,[25] anti-counterfeiting,[26] and display devices.[27] In addition, afterglow room temperature phosphorescence (RTP) has attracted significant attention due to its long lifetime, large Stokes shift and wide applicability. As such, RTP is often applied for use in chemical sensing,[28] biological imaging,[29] and photoelectric conversion.[30]

With this research, we observe that technical lignin (lignin sulfonate), found as a main component of black liquor produced during the pulping process,[31] exhibits phosphorescence emission in aqueous solution. The lifetime of the LS phosphorescence is ~2 ms. Moreover, we find that an afterglow material with a long lifetime of ~618 ms can be obtained by embedding LS in an inorganic $Ca_3(PO_4)_2$ matrix (LS@$Ca_3(PO_4)_2$), due to H-type dimers of the S units (4-hydroxy-3,5-dimethoxybenzoic unit) of LS forming within $Ca_3(PO_4)_2$. As such, LS@$Ca_3(PO_4)_2$ could be used as a paper additive for the generation of afterglow emission. To begin with, we prepare the inorganic matrix by dispersing $Ca_3(PO_4)_2$ powder in ethanol facilitated by the addition of triethylamine as a ligand to prepare calcium phosphate oligomers (CPO) (Figure 1A).[32] The CPO is then mixed with LS, and paper pulp (Figure 1A). Subsequently, the mixed solution is filtered, and the solid residues are heated to promote crosslinking of the CPO by removal of the triethylamine (Figure 1A). This process results in the *in situ* generation of LS@$Ca_3(PO_4)_2$-coated paper pulp fibers (Figure 1A). Significantly, the paper produced by this method exhibits afterglow emission (Figure 1B). Due to the easy processability of paper (by folding, etc.), the

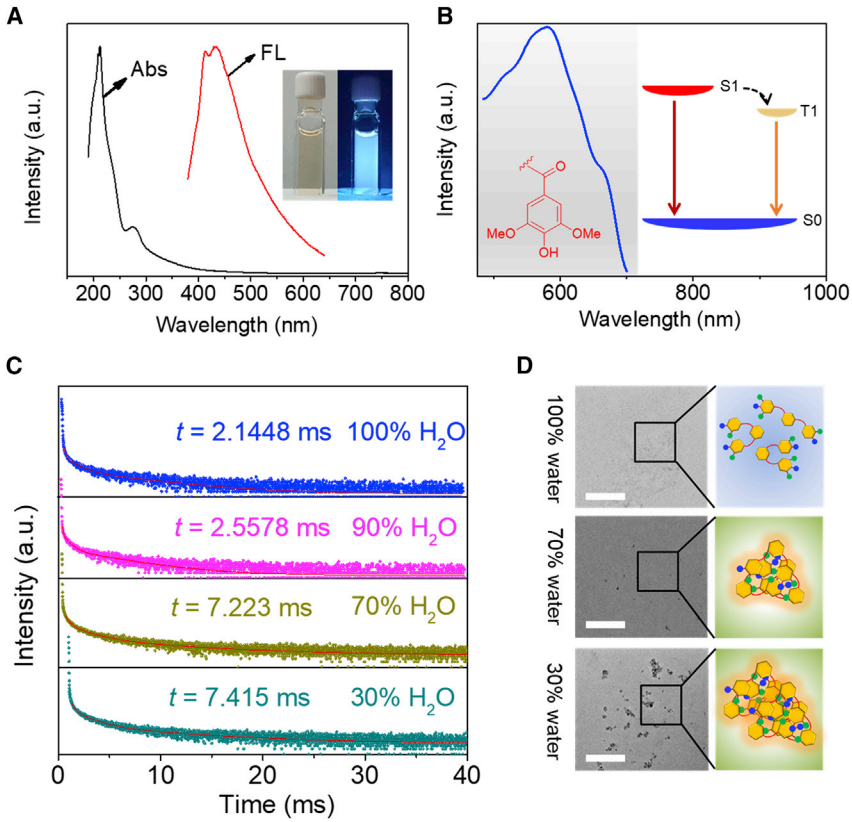

Figure 2. Phosphorescence of LS in aqueous solution

(A) Absorbance and fluorescence of LS in water solution (excitation wavelength = 365 nm).

(B) Phosphorescence spectra of LS at 25°C, (inset) proposed chromophore.

(C) Lifetime of LS in a mixture of water and ethanol (excitation wavelength = 365 nm).

(D) TEM images of LS in the mixture of water and ethanol. Scale bar, 200 nm.

afterglow paper can be easily converted into an emissive construct of any desired shape. In addition, the afterglow emission of the paper can be efficiently quenched by H_2O_2, facilitating its application as a sensor for H_2O_2. Furthermore, the afterglow paper can be used for anti-counterfeiting purposes.

RESULTS AND DISCUSSION

Phosphorescence of LS in aqueous solution

The ultraviolet-visible (UV-Vis) spectra of LS exhibits optical absorbance predominantly in the UV-Vis region in water solution, over a wavelength range from 200 nm to 500 nm (Figure 2A). Upon UV irradiation, LS exhibited strong fluorescence emission, centered at 440 nm in water solution (Figure 2A, inset). Surprisingly, LS also exhibited phosphorescence emission centered at ~570 nm (Figure 2B). To determine the chromophore responsible for the emission, the structure of LS was determined using two-dimensional heteronuclear singular quantum correlation nuclear magnetic resonance spectroscopy (2D HSQC NMR) (Figure S1). The NMR spectra indicated that LS contained G, S, H, and polymerized units. Discrete Fourier transform (DFT) calculations indicated that the S unit (4-hydroxy-3,5-dimethoxybenzoic moieties) in LS exhibited an energy gap of ~2.1 eV between the triplet state and ground state, which matched well with the corresponding emission peak at ~570 nm in the phosphorescence spectra (Figure 2B). To further illustrate this point, the phosphorescence spectra of a model compound, 4-hydroxy-3,5-dimethoxybenzoic acid,

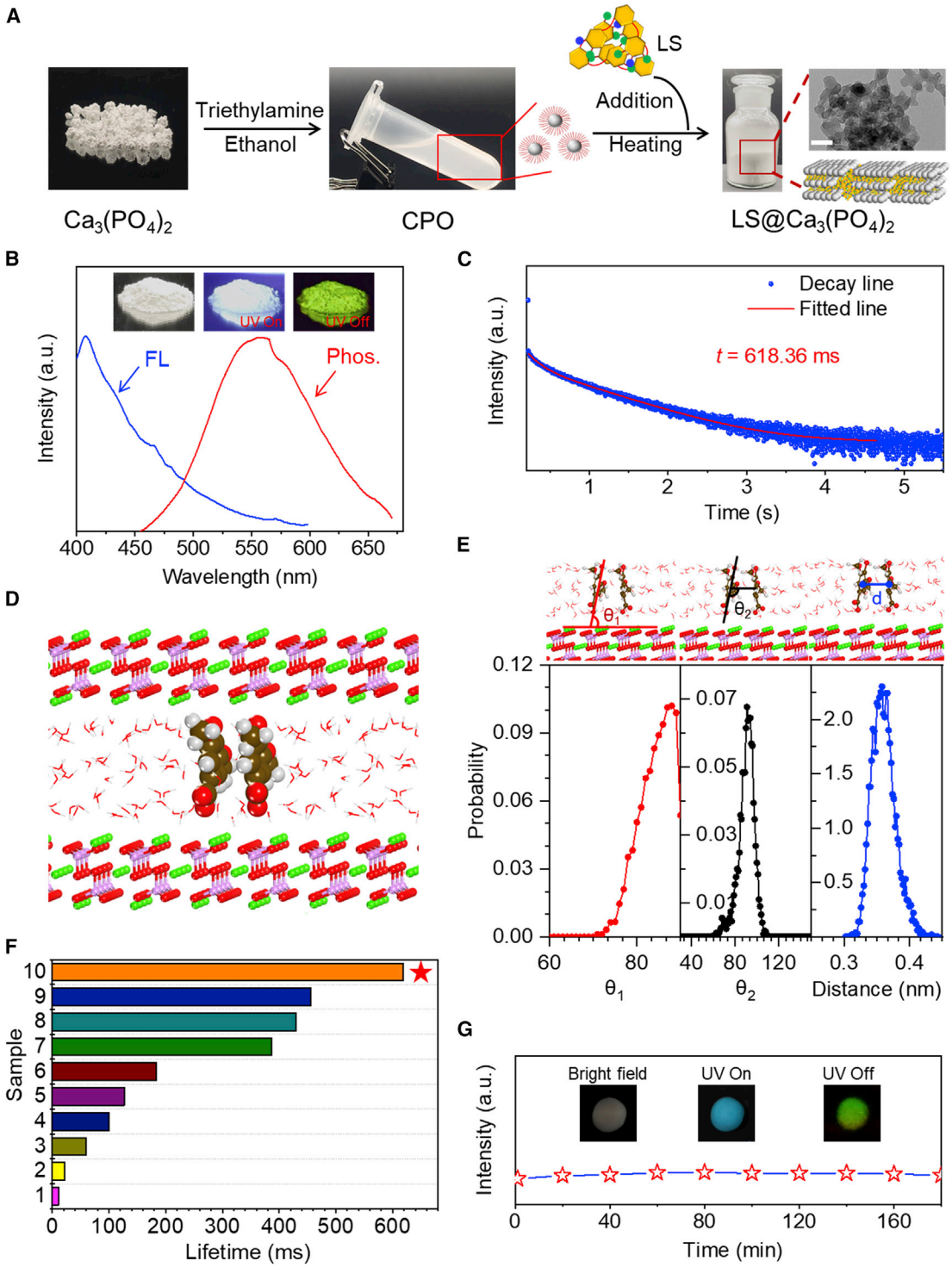

Figure 3. Afterglow emission of LS@$Ca_3(PO_4)_2$

(A) Schematic illustration of the preparation of LS@$Ca_3(PO_4)_2$. TEM images of LS@$Ca_3(PO_4)_2$. Scale bar, 50 nm.

(B) Fluorescence emission and phosphorescence emission of LS@$Ca_3(PO_4)_2$ upon 365-nm excitation. (Inset) images of powdered LS@$Ca_3(PO_4)_2$ upon UV excitation.

(C) Lifetime of LS@$Ca_3(PO_4)_2$.

(D) Distribution of model LS in $Ca_3(PO_4)_2$.

was measured and similar phosphorescence emission was observed (Figure S2), confirming that the S unit in the LS was in fact the chromophore responsible for the phosphorescence emission. The lifetime of the phosphorescence in water solution was ~2 ms (Figure 2C). Interestingly, the lifetime of the phosphorescence increased from ~2.1 ms to ~7.4 ms upon addition of ethanol (a poor solvent for LS) with increasing fractions from 0% to 70%. However, no afterglow emission was observed by the naked eye (Figure S3). Meanwhile, the scanning electron microscopy (SEM) images indicated that LS aggregates increased upon increasing the fraction of ethanol in the mixed solvent (Figure 2D). This is because LS is hydrophilic and the solubility of LS is poor in ethanol. Therefore, the addition of ethanol triggered the shrinkage of LS, which drives molecular aggregation.[33] These factors suggest a possible mechanism for the phosphorescence of LS in aqueous solution: the LS was well dissolved in water solution and the triplet state of the S unit was quenched by water, and therefore exhibited short-lived phosphorescence. However, upon the addition of a poor solvent, the LS molecules formed aggregates and the S units in LS were protected inside these aggregates, resulting in stabilized triplet states with longer lived phosphorescence.

Afterglow emission of LS@$Ca_3(PO_4)_2$

Inspired by the enhanced phosphorescence of aggregated LS, an inorganic matrix, $Ca_3(PO_4)_2$, was used to protect the S unit in LS to extend the phosphorescence lifetime (Figure 3A). To this end, CPO was dispersed in ethanol stabilized by triethylamine as a ligand. The CPO was then mixed with a water solution of LS. Subsequently, the mixed solution was heated at 120°C to evaporate the solvent and triethylamine, triggering the crosslinking of CPO and confining the LS within $Ca_3(PO_4)_2$. This process resulted in the generation of LS@$Ca_3(PO_4)_2$ as a white powder (Figure 3A). Transmission electron microscopy (TEM) and elemental imaging of the LS@$Ca_3(PO_4)_2$ indicated that the LS was well dispersed within the matrix of $Ca_3(PO_4)_2$ (Figure 3A). A cross-sectional view of LS@$Ca_3(PO_4)_2$ indicated that LS was confined between layers of $Ca_3(PO_4)_2$ (Figure S4). Simulation of the small-angle X-ray scattering (SAXS) spectra further confirmed the morphology. Guinier-Porod model fitting of the SAXS curve suggests that $Ca_3(PO_4)_2$ in LS@$Ca_3(PO_4)_2$ has a lamella shape, which is consistent with the TEM results (Figure S5).[34] More interestingly, the simulation also suggests that the thickness of the lamella of $Ca_3(PO_4)_2$ decreases from ~13 nm to ~8.6 nm upon addition of LS. This was because LS entered the layer of $Ca_3(PO_4)_2$ lamella, preventing the intensive packing of $Ca_3(PO_4)_2$. However, this process does not destroy the crystalline structure of $Ca_3(PO_4)_2$, as pure $Ca_3(PO_4)_2$ (dried from CPO) and LS@$Ca_3(PO_4)_2$ exhibit a similar XRD pattern (Figure S5). All these results confirmed that the LS was confined and protected by the $Ca_3(PO_4)_2$ (Figure 3A). As expected, LS@$Ca_3(PO_4)_2$ exhibited strong afterglow emission centered at ~550 nm, which was a shorter wavelength than the pure LS (Figure 3B). Control experiments confirmed that $Ca_3(PO_4)_2$ alone did not produce afterglow emission and exhibited a short lifetime of 11.4 ns (Figure S6). These results indicated that embedding LS into $Ca_3(PO_4)_2$ resulted in afterglow emission with an extended lifetime. The lifetime of LS@$Ca_3(PO_4)_2$ was ~618 ms (Figure 3C). To further understand the extended afterglow, theoretical calculations were used to determine the molecular dispersion in $Ca_3(PO_4)_2$. To simplify the system, 4-hydroxy-3,5-dimethoxybenzoic acid was used as the model chromophore of lignin. It was

(E) Distribution of angles and distance for model LS in $Ca_3(PO_4)_2$.
(F) Comparison of lifetime between LS@$Ca_3(PO_4)_2$ (sample 10) and the reported sustainable samples.
(G) Phosphorescence intensity of LS@$Ca_3(PO_4)_2$ in water. (Inset) images of LS@$Ca_3(PO_4)_2$ in a water droplet upon UV excitation. See also Video S1.

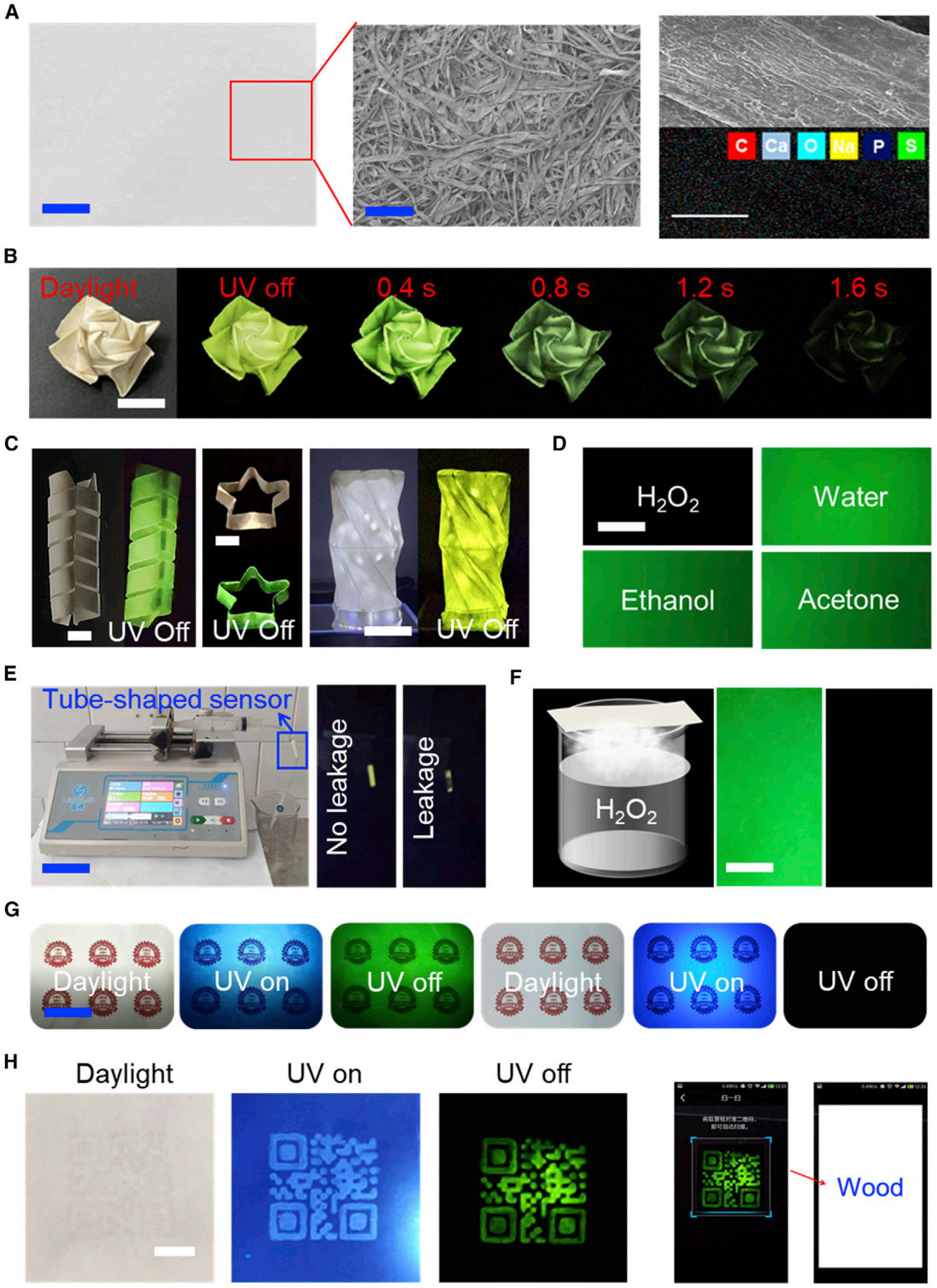

Figure 4. Application of afterglow paper

(A) Digital (scale bar, 5 cm), SEM images (scale bar, 100 μm), and elemental mapping (scale bar, 10 μm) of afterglow paper.

(B) Digital images of a flower made from afterglow paper after switching off the UV sources. Scale bar, 1 cm.

(C) Digital images of 3D constructs made using afterglow paper after switching off the UV sources. Scale bar, 1 cm (left and middle), scale bar, 5 cm (right).

observed that H-type 4-hydroxy-3,5-dimethoxybenzoic acid dimers formed between the $Ca_3(PO_4)_2$ nanosheets (Figure 3D). Specifically, the most probable angle for the chromophore of lignin relative to the $Ca_3(PO_4)_2$ monolayer appears at ~85° (θ_1) (Figure 3E). In addition, the results indicated that the average center-center distance between adjacent molecules was ~0.35 nm, which facilitated the formation of strong π - π interactions between the layers of the phosphors (Figure 3E). The relative orientation of two neighboring 4-hydroxy-3,5-dimethoxybenzoic acids (θ_2) was mainly populated over a range from ~60° to 100° with an optimal angle of ~90°, and this stacking is what caused the phosphorescence blue-shift of the LS@$Ca_3(PO_4)_2$ compared with pure LS. There are two types of aromatic aggregates including J-type aggregates and H-type aggregates. J-type aggregates are formed when the angle between the transition dipoles and the interconnected axis is smaller than the critical value of 54.7°($\theta < 54.7°$). H-type aggregates are formed when the angle between the transition dipoles and the interconnected axis is larger than the critical value of 54.7°($\theta > 54.7°$).[35] Therefore, LS formed H-aggregates in this matrix. Such H-aggregates can stabilize the lowest excited triplet states, and prolong the RTP lifetime.[35,36] To further prove the theoretical calculation, the RTP properties of 4-hydroxy-3,5-dimethoxybenzoic acid @$Ca_3(PO_4)_2$ were evaluated. As expected, 4-hydroxy-3,5-dimethoxybenzoic acid @$Ca_3(PO_4)_2$ exhibited an RTP emission centered at 550 nm with a lifetime of 341 ms (Figure S7). Comparison between reported sustainable afterglow materials and our results indicated that the LS@$Ca_3(PO_4)_2$ exhibited the longest lifetime (Figure 3F).[37–45] To illustrate the general applicability of our strategy, LS was then embedded into $CaCO_3$ and $CaSO_4$ to produce afterglow materials, respectively.[46] LS@$CaCO_3$ and LS@$CaSO_4$ exhibited a rod and cubic-like morphology, respectively (Figure S8). Fortuitously, both LS@$CaCO_3$ and LS@$CaSO_4$ produced efficient afterglow emissions (Figures S9 and S10). Then the stability of LS@$Ca_3(PO_4)_2$ in aqueous solution was evaluated. A nice afterglow emission was observed when LS@$Ca_3(PO_4)_2$ was immersed in water, and this was stable for over 2 h (Figure 3G and Video S1). Moreover, LS@$Ca_3(PO_4)_2$ exhibited afterglow emission in acidic and basic water solutions as well as organic solvents (Figure S11). These results confirmed that LS@$Ca_3(PO_4)_2$ not only exhibited afterglow emission in the solid state, but also exhibited stable afterglow emission in an aqueous solution.

Applications

In order to demonstrate the applicability of the system, LS@$Ca_3(PO_4)_2$ was used as an additive to develop afterglow paper. CPO was mixed with LS and paper pulp. Then, the mixed solution was filtered and the solid residue was heated to promote crosslinking of the CPO through removal of the triethylamine. As such, the LS@$Ca_3(PO_4)_2$ generated *in situ* coated the surface of the paper pulp fibers (Figure 4A). As a control, paper without LS@$Ca_3(PO_4)_2$ contained only C and O elements, which are from the cellulose (Figure S12). Significantly, the LS@$Ca_3(PO_4)_2$ enhanced the mechanical performance of the afterglow paper (Figures 4A and S13), which we attribute to hydrogen bonding interaction between the cellulose and LS@$Ca_3(PO_4)_2$.[47] The paper exhibited nice afterglow emission upon UV irradiation with a lifetime of ~105.6 ms (Figures 4B and S14). As a control, paper without LS@$Ca_3(PO_4)_2$ did not display any afterglow RTP emission

(D) Afterglow emission of the paper after UV excitation treated with liquid H_2O_2 (0.1%), water, ethanol and acetone. Scale bar, 2 cm.
(E) Setup of transportation line for liquid H_2O_2 decorated with paper tube-shape sensor (left), images of afterglow emission of the sensor without/with the leakage of liquid H_2O_2 (middle and right). Scale bar, 10 cm.
(F) Afterglow emission of the paper before and after treatment of H_2O_2 vapor. Scale bar, 1 cm.
(G) Printed afterglow paper (left) and normal paper (right) upon and after UV irradiation. Scale bar, 5 cm.
(H) Two-dimensional code image made from LS@$Ca_3(PO_4)_2$ on paper upon and after UV irradiation. Scale bar, 1 cm. See also Video S2.

(Figure S15). Interestingly, the afterglow paper can be written on using a UV laser (Video S2). The afterglow paper can also be processed into 3D afterglow devices with different shapes (Figure 4C). Remarkably, the afterglow paper exhibited sensitive afterglow quenching when exposed to the liquid H_2O_2 (Figure 4D). As a control, the paper did not show afterglow quenching upon treatment with water, acetone, or ethanol (Figure 4D). This phenomenon was attributed to the quenching of the triplet state in LS@$Ca_3(PO_4)_2$ by H_2O_2.[48] The good sensitivity, combined with ease of processability, enabled the application of the afterglow as a sensor for detecting H_2O_2 leakage. Therefore, we prepared tube-shaped afterglow paper that was then coated to the outside of a transportation line for H_2O_2. The sensor exhibited nice afterglow emission when the transportation line did not show leakage. However, when leakage occurred, afterglow emission was quenched (Figure 4E). Moreover, the afterglow paper also exhibited a good response to H_2O_2 vapor. Exposure of the afterglow paper to H_2O_2 vapor for 1 s efficiently quenched its afterglow emission (Figure 4F). These results confirmed that our afterglow paper provided an alternative cheap and efficient way for sensing H_2O_2 both in the liquid and vapor states, which is currently an important issue in anti-terrorism and industrial healthcare issues, etc.[49] After that, the afterglow paper was investigated for anti-counterfeiting applications. To that end, the afterglow paper was printed on using a commercial printer. Importantly, the afterglow emission remained after the paper was printed upon (Figure 4G). As a control, no afterglow emission was observed for printed normal paper (Figure 4G). In addition, the mixture of LS and CPO can also be used as afterglow inks for printing on normal paper suitable for anti-counterfeiting purposes. Therefore, we printed a 2D code using LS/CPO mixture (LS: 10 mg/mL, CPO: 20 mg/mL) onto normal paper. After that, the paper was heated at 120°C for 3 min to trigger the *in situ* generation of afterglow LS@$Ca_3(PO_4)_2$. In this way, on UV irradiation, the paper displayed a nice 2D fluorescent code. In addition, a high-resolution RTP code was observed after switching off the UV source. More importantly, the RTP code could be recognized using a smart phone (Figure 4H). All these results confirmed that the flexible afterglow paper exhibited significant potential for sensing H_2O_2 and anti-counterfeiting purposes.

In summary, we have been able use lignin to generate valuable additives for the pulp and paper industry. The afterglow emission of LS was significantly extended by promoting the formation of H-type dimmers of the S units in LS through confinement within a matrix of $Ca_3(PO_4)_2$. The as-prepared LS@$Ca_3(PO_4)_2$ could then be used as an afterglow ink suitable for anti-counterfeiting applications. In addition, we have demonstrated the utility of the matrix confinement approach by creating LS@$Ca_3(PO_4)_2$ *in situ* during the paper fabrication process to produce afterglow paper suitable for H_2O_2 sensing. Importantly, this research has demonstrated that functional afterglow paper can be generated using lignin produced directly by the pulp and paper industry, removing the need for additional transportation or expensive treatment. Given the convenient preparation and low price of the inorganic matrix, our strategy can be easily incorporated into the current production line via minor modification. We anticipate that this research will encourage the development of new practical strategies for enabling an efficient utilization of lignin toward a more sustainable paper and pulp industry.

EXPERIMENTAL PROCEDURES

Resource availability

Lead contact

Further information and requests for resources and reagents should be directed to and will be fulfilled by the lead contact, Zhijun Chen (e-mail: chenzhijun@nefu.edu.cn).

Materials availability

Sodium lignosulfonate was purchased from Aladdin (Shanghai, China) and used as received without further purification. Anhydrous calcium chloride was purchased from Tianjin Hengxing Chemical Reagent Manufacturing Co., LTD. Ethanol was purchased from Tianjin Tianli Chemical Reagent Co., Ltd. (Tianjin, China). Phosphoric acid and triethylamine were purchased from Tianjin Kemiou Chemical Reagent Co., LTD. Anhydrous sodium sulfate and anhydrous sodium carbonate were purchased from Tianjin Tianli Chemical Reagent Co., LTD and Tianjin Beichen Founder Reagent. All were analytically pure reagents. Various anhydrous reagents, water $\leq$ 50 ppm (including anhydrous dimethyl sulfoxide, anhydrous dimethylformamide, anhydrous acetonitrile, anhydrous tetrahydrofuran, and anhydrous ethanol) were purchased from Macklin (Shanghai, China). Deionized water, prepared using a Master Q30UT water purification system (Hitech Instruments Co. Ltd., Shanghai, China), was used in all experiments. Pulp was purchased from Alibaba (Hangzhou, China).

Data and code availability

Data supporting the findings of this paper are available as supplemental items, and any additional information required to reanalyze the data reported in this paper is available from the lead contact upon request.

Characterization

SEM images were obtained using a Gemini SEM 300 field emission scanning electron microscope (ZEISS Co., Ltd., Germany). TEM images were obtained using an HT7700 transmission electron microscope (Hitachi Co., Ltd., Japan), at an operating voltage of 100 kV. The afterglow spectra and lifetime decay curves of the samples were recorded using NanoLog infrared fluorescence spectrometer (HORIBA Scientific, Model Nanolog FL3-2IHR, US) and Ultra Fast Lifetime Spectrofluorometer instrument, (DeltaFlex, Horiba Jobinyvon IBH Inc., UK), equipped with a xenon lamp and a microsecond flashlamp (detector: photomultiplier tube, λ = 200–1700 nm). Fluorescence was measured using a FluoroMax-4 spectrofluorometer (Horiba, Edison, NJ). UV-Vis absorption spectra were recorded using a TU-1901 UV-Vis double-beam spectrophotometer (Persee General Instrument Co., Ltd., Beijing, China). 2D-HSQC NMR spectra were recorded using an AVANCE 600 MHz spectrometer (Bruker, Germany). The X-ray Small-Angle Scatterer (SAXS/WAXS) was evaluated using solid SAXS instrument of The Brooke Nano STAR U SAXS model. The parameters were 50 kV, 0.6 mA, and the X-ray wavelength was 0.154 nm. Paper whiteness is tested using a whiteness color tester, model YQ-Z-48A. Paper mechanics were evaluated using an electronic universal testing machine, model UTM2203, maximum test force is 2kN.

Synthesis of LS@$Ca_3(PO_4)_2$

4.704 g of anhydrous calcium chloride was dissolved in 1.6 L ethanol to form a transparent alcohol solution, 88.716 mL triethylamine was added and stirred at room temperature for 30 min, 1.672 mL H_3PO_4 was dissolved in 80 mL of ethanol, and then slowly added to the above solution, which was stirred at room temperature for 12 h, and centrifuged at 8000 rpm/min to obtain the CPO gel. CPO gel was then dispersed in ethanol to form a homogeneous emulsion at a concentration of 20 mg/mL. 40 mL of CPO solution was then mixed with 0.2 mL sodium lignosulfonate solution (concentration: 10 mg/mL) and centrifuged at 8000 rpm/min for 15 min to obtain LS@CPO gel, which was dried at 90 degrees to obtain LS@$Ca_3(PO_4)_2$ powder.

Preparation of LS@$CaCO_3$

20 mL of $CaCl_2$ saturated solution was added to a 50 mL centrifuge tube with a pipette, and 0.2 mL sodium lignosulfonate solution (concentration: 10 mg/mL)

was added and mixed. Then 20 mL $NaCO_3$ saturated solution was added and the precipitate centrifuged at 8000 rpm/min for 15 min. The supernatant was then removed and the precipitate was dried in a 90-degree oven to obtain LS@$CaCO_3$.

Preparation of LS@$CaSO_4$

20 mL of $CaCl_2$ saturated solution was added to a 50 mL centrifuge tube with a pipette, and 0.2 mL sodium lignosulfonate solution (concentration: 10 mg/mL) was added to mix evenly. Then 20 mL Na_2SO_4 saturated solution was added and the precipitate centrifuged at 8000 rpm/min for 15 min. The supernatant was then removed and the precipitate was dried in a 90-degree oven to obtain LS@$CaSO_4$.

Preparation of afterglow paper

250 mL of deionized water was added to 7.4 g paper pulp, which was then stirred until evenly dispersed. Then 20 mL CPO suspension, 5 mL LS solution (concentration: 10 mg/mL), and 3 mL Arabic gum solution (concentration: 5 mg/mL) were added to the pulp solution. After stirring, the dispersion was then filtered. The afterglow paper was obtained after pressing and baking the solid residue.

Computational methods

DFT was used to investigate the molecular energy gap using the Gaussian 16 program.[50] Geometry optimization calculations were performed using the B3LYP-D3 DFT method.[51–53] To determine the distribution of 4-hydroxy-3,5-dimethoxybenzoic acid in $Ca_3(PO_4)_2$, a $Ca_3(PO_4)_2$ supercell was constructed, with lattice parameters a = 36.36 Å, b = 31.49 Å, $\alpha = \beta = \gamma = 90^{\circ}$, containing 432 Ca^{2+}, 288 PO_4^{3-}. The supercell was treated as having P1 symmetry and all the lattice parameters were considered as independent variables in the simulation. A 3D periodic boundary condition[54] was applied to the whole system. Then, eight 4-hydroxy-3,5-dimethoxybenzoic acids were introduced into the supercell, with their carboxylic groups vertical to the $Ca_3(PO4)_2$ layers. According to the experimental elemental analysis, 300 water molecules were inserted into the simulated supercell based on the rule that these molecules occupy the whole available interlayer space as much as possible. As a result, the formula of the simulated structure can be expressed as $(Ca_3(PO4)_2)_{144}(C_9H_{10}O_5)_8\bullet 300H_2O$. Then, MD calculations were performed by a classical molecular dynamic simulation method employing a modified cff91 force field.[55] A charge equilibration (QEq) method[56] was used to calculate the atomic charges of the layer. Other forcefield parameters for the anions were obtained from the cff91 forcefield.[57] After energy minimization was applied to the initial model, MD simulations were performed in an isothermal–isobaric (NPT) ensemble with a typical thermodynamic temperature of 273 K and typical pressures of 0.1 MPa. The Andersen method[58] and Berendsen method[59] were used to control temperature and pressure, respectively. The total simulation time was 1,000 ps with a simulation time step of 0.1 fs. The simulations were performed using the Forcite module in the Material Studio software package.[60]

Preparation of 2D code

A 2D code template was used. LS/CPO mixtures were sprayed onto the paper through the template. After hot pressing, the template was removed and a 2D code was formed on the paper.

SUPPLEMENTAL INFORMATION

Supplemental information can be found online at https://doi.org/10.1016/j.xcrp.2022.100867.

ACKNOWLEDGMENTS

This work was supported by the National Natural Science Foundation of China (31890774 and 31800494), Special Project for Double First-Class—Cultivation of Innovative Talents, (000/41113102), Natural Science Funding of Heilong Jiang Province for Excellent Young Scholars (YQ2020C017), Excellent Young Scholar Sponsorship Program by National Forestry and Grassland Administration of China Funding (2019132611), the Heilongjiang Postdoctoral Science Foundation (LBH-Z18005), and the Young Elite Scientists Sponsorship Program by CAST (2018QNRC001). T.D.J. thanks the Royal Society for a Wolfson Research Merit Award and the Open Research Fund of the School of Chemistry and Chemical Engineering, Henan Normal University for support (2020ZD01).

AUTHOR CONTRIBUTIONS

Z.C., M.L., and T.D.J. developed the concept. M.M.Y. and H.L. conducted the experiments and the simulation. J.S. prepared the afterglow paper. Z.C., M.L., S. Li, S. Liu, J.L., and T.D.J. wrote the paper.

DECLARATION OF INTERESTS

The authors have no competing interests.

Received: January 20, 2022
Revised: February 27, 2022
Accepted: March 31, 2022
Published: April 22, 2022

REFERENCES

1. Kong, L., Hasanbeigi, A., and Price, L. (2016). Assessment of emerging energy-efficiency technologies for the pulp and paper industry: a technical review. J. Clean. Prod. *122*, 5–28.
2. Bajpai, P. (2015). Green Chemistry and Sustainability in Pulp and Paper Industry (Springer).
3. Balakshin, M.Y., Capanema, E.A., Sulaeva, I., Schlee, P., Huang, Z., Feng, M., Borghei, M., Rojas, O.J., Potthast, A., and Rosenau, T. (2021). New opportunities in the valorization of technical lignins. ChemSusChem *14*, 1016–1036.
4. Xia, Z., Li, J., Zhang, J., Zhang, X., Zheng, X., and Zhang, J. (2020). Processing and valorization of cellulose, lignin and lignocellulose using ionic liquids. J.Bioresour.Bioprod. *5*, 79–95.
5. Vishtal, A., and Kraslawski, A. (2011). Challenges in industrial applications of technical lignins. Bioresources *6*, 3547–3568.
6. Aro, T., and Fatehi, P. (2017). Production and application of lignosulfonates and sulfonated lignin. ChemSusChem *10*, 1861–1877.
7. Li, C., Zhao, X., Wang, A., Huber, G.W., and Zhang, T. (2015). Catalytic transformation of lignin for the production of chemicals and fuels. Chem. Rev. *115*, 11559–11624.
8. Guo, H., Zhang, B., Qi, Z., Li, C., Ji, J., Dai, T., Wang, A., and Zhang, T. (2017). Valorization of lignin to simple phenolic compounds over tungsten carbide: impact of lignin structure. ChemSusChem *10*, 523–532.
9. Wang, M., and Wang, F. (2019). Catalytic scissoring of lignin into aryl monomers. Adv.Mater. *31*, 1901866.
10. Xu, C., Arancon, R.A.D., Labidi, J., and Luque, R. (2014). Lignin depolymerisation strategies: towards valuable chemicals and fuels. Chem. Soc. Rev. *43*, 7485–7500.
11. Hatakeyama, H., and Hatakeyama, T. (2009). Lignin structure, properties, and applications. Biopolymers *203*, 1–63.
12. Shu, F., Jiang, B., Yuan, Y., Li, M., Wu, W., Jin, Y., and Xiao, H. (2021). Biological activities and emerging roles of lignin and lignin-based products—a review. Biomacromolecules *22*, 4905–4918.
13. Prabhu, P., Wan, Y., and Lee, J.-M. (2020). Electrochemical conversion of biomass derived products into high-value chemicals. Matter *3*, 1162–1177.
14. Bruijnincx, P.C.A., and Weckhuysen, B.M. (2014). Biomass conversion Lignin up for breakdown. Nat. Chem. *6*, 1035–1036.
15. Ragauskas, A.J., Williams, C.K., Davison, B.H., Britovsek, G., Cairney, J., Eckert, C.A., Frederick, W.J., Hallett, J.P., Leak, D.J., and Liotta, C.L. (2006). The path forward for biofuels and biomaterials. Science *311*, 484–489.
16. Xia, Q., Chen, C., Yao, Y., He, S., Wang, X., Li, J., Gao, J., Gan, W., Jiang, B., and Cui, M. (2021). In situ lignin modification toward photonic wood. Adv.Mater. *33*, 2001588.
17. Österberg, M., Sipponen, M.H., Mattos, B.D., and Rojas, O.J. (2020). Spherical lignin particles: a review on their sustainability and applications. Green. Chem. *22*, 2712–2733.
18. Zhao, X., Huang, C., Xiao, D., Wang, P., Luo, X., Liu, W., Liu, S., Li, J., Li, S., and Chen, Z. (2021). Melanin-inspired design: preparing sustainable photothermal materials from lignin for energy generation. ACS Appl. Mater. Inter. *13*, 7600–7607.
19. Li, J., Liu, W., Qiu, X., Zhao, X., Chen, Z., Yan, M., Fang, Z., Li, Z., Tu, Z., and Huang, J. (2022). Lignin: a sustainable photothermal block for smart elastomers. Green. Chem. *24*, 823–836. https://doi.org/10.1039/D1GC03571A.
20. Xue, Y., Qiu, X., Wu, Y., Qian, Y., Zhou, M., Deng, Y., and Li, Y. (2016). Aggregation-induced emission: the origin of lignin fluorescence. Polym. Chem. *7*, 3502–3508.
21. Ma, Z., Liu, C., Niu, N., Chen, Z., Li, S., Liu, S., and Li, J. (2018). Seeking brightness from nature: J-aggregation-induced emission in cellulolytic enzyme Lignin nanoparticles. ACS Sustain. Chem. Eng. *6*, 3169–3175.
22. Li, W., Chen, Z., Yu, H., Li, J., and Liu, S. (2021). Wood-derived carbon materials and light-emitting materials. Adv. Mater. *33*, 2000596.
23. Yuan, J., Zhai, Y., Wan, K., Liu, S., Li, J., Li, S., Chen, Z., and James, T.D. (2021). Sustainable

afterglow materials from lignin inspired by wood phosphorescence. Cell Rep. Phys. Sci. *2*, 100542.

24. Mahadeva, S.K., Walus, K., and Stoeber, B. (2015). Paper as a platform for sensing applications and other devices: a review. ACS Appl. Mater. Inter. *7*, 8345–8362.

25. Duan, Z., Jiang, Y., Yan, M., Wang, S., Yuan, Z., Zhao, Q., Sun, P., Xie, G., Du, X., and Tai, H. (2019). Facile, flexible, cost-saving, and environment-friendly paper-based humidity sensor for multifunctional applications. ACS Appl. Mater. Inter. *11*, 21840–21849.

26. She, P., Ma, Y., Qin, Y., Xie, M., Li, F., Liu, S., Huang, W., and Zhao, Q. (2019). Dynamic luminescence manipulation for rewritable and multi-level security printing. Matter *1*, 1644–1655.

27. Zhao, X., Han, W., Zhao, C., Wang, S., Kong, F., Ji, X., Li, Z., and Shen, X. (2019). Fabrication of transparent paper-based flexible thermoelectric generator for wearable energy harvester using modified distributor printing technology. ACS Appl. Mater. Inter. *11*, 10301–10309.

28. Su, Q., Lu, C., and Yang, X. (2019). Efficient room temperature phosphorescence carbon dots: information encryption and dual-channel pH sensing. Carbon *152*, 609–615.

29. Dang, Q., Jiang, Y., Wang, J., Wang, J., Zhang, Q., Zhang, M., Luo, S., Xie, Y., Pu, K., Li, Q., et al. (2020). Room-temperature phosphorescence resonance energy transfer for construction of near-infrared afterglow imaging agents. Adv. Mater. *32*, 2006752.

30. Wang, J., Liang, B., Wei, J., Li, Z., Xu, Y., Yang, T., Li, C., and Wang, Y. (2021). Highly efficient electrofluorescence material based on pure organic phosphor sensitization. Angew. Chem. Int. Ed. *60*, 15335–15339.

31. Shi, H., Fatehi, P., Xiao, H., and Ni, Y. (2011). A combined acidification/PEO flocculation process to improve the lignin removal from the pre-hydrolysis liquor of kraft-based dissolving pulp production process. Bioresour. Technol. *102*, 5177–5182.

32. Yu, Y., Mu, Z., Jin, B., Liu, Z., and Tang, R. (2020). Organic–inorganic copolymerization for a homogenous composite without an interphase boundary. Angew. Chem. Int. Ed. *59*, 2071–2075.

33. Zhao, W., Simmons, B., Singh, S., Ragauskas, A., and Cheng, G.J.G.C. (2016). From lignin association to nano-/micro-particle preparation: extracting higher value of lignin. Green. Chem. *18*, 5693–5700.

34. Hammouda, B. (2010). A new Guinier–Porod model. J. Appl. Crystallogr. *43*, 716–719.

35. An, Z., Zheng, C., Tao, Y., Chen, R., Shi, H., Chen, T., Wang, Z., Li, H., Deng, R., Liu, X., et al. (2015). Stabilizing triplet excited states for ultralong organic phosphorescence. Nat. Mater. *14*, 685–690.

36. Gao, R., and Yan, D. (2017). Layered host–guest long-afterglow ultrathin nanosheets: high-efficiency phosphorescence energy transfer at 2D confined interface. Chem. Sci. *8*, 590–599.

37. Green, D.C., Holden, M.A., Levenstein, M.A., Zhang, S., Johnson, B.R., de Pablo, J.G., Ward, A., Botchway, S.W., and Meldrum, F.C. (2019). Controlling the fluorescence and room-temperature phosphorescence behaviour of carbon nanodots with inorganic crystalline nanocomposites. Nat. Commun. *10*, 1–13.

38. Bai, L.Q., Xue, N., Wang, X.R., Shi, W.Y., and Lu, C. (2017). Activating efficient room temperature phosphorescence of carbon dots by synergism of orderly non-noble metals and dual structural confinements. Nanoscale *9*, 6658–6664.

39. Su, Q., and Yang, X. (2021). Promoting room temperature phosphorescence through electron transfer from carbon dots to promethazine. ACS Appl. Mater. Inter. *13*, 41238–41248.

40. Wang, B., Yu, Y., Zhang, H., Xuan, Y., Chen, G., Ma, W., Li, J., and Yu, J. (2019). Carbon dots in a matrix: energy-transfer-enhanced room-temperature red phosphorescence. Angew. Chem. Int. Ed. *131*, 18614–18619.

41. Tian, Z., Li, D., Ushakova, E.V., Maslov, V.G., Zhou, D., Jing, P., Shen, D., Qu, S., and Rogach, A.L. (2018). Multilevel data encryption using thermal-treatment controlled room temperature phosphorescence of carbon dot/polyvinylalcohol composites. Adv. Sci. *5*, 1800795.

42. Jiang, K., Gao, X., Feng, X., Wang, Y., Li, Z., and Lin, H. (2020). Carbon dots with dual-emissive, robust, and aggregation-induced room-temperature phosphorescence characteristics. Angew. Chem. Int. Ed. *132*, 1279–1285.

43. Wang, B., Mu, Y., Zhang, H., Shi, H., Chen, G., Yu, Y., Yang, Z., Li, J., and Yu, J. (2019). Red room-temperature phosphorescence of CDs@zeolite composites triggered by heteroatoms in zeolite frameworks. ACS Cent. Sci. *5*, 349–356.

44. Jiang, K., Zhang, L., Lu, J., Xu, C., Cai, C., and Lin, H. (2016). Triple-mode emission of carbon dots: applications for advanced anti-counterfeiting. Angew. Chem. Int. Ed. *128*, 7347–7351.

45. Jiang, K., Sun, S., Zhang, L., Lu, Y., Wu, A., Cai, C., and Lin, H. (2015). Red, green, and blue luminescence by carbon dots: full-color emission tuning and multicolor cellular imaging. Angew. Chem. Int. Ed. *127*, 5450–5453.

46. Liu, H., Zhu, J., and Fu, S. (2010). Effects of lignin-metal complexation on enzymatic hydrolysis of cellulose. J. Agric. Food Chem. *58*, 7233–7238.

47. Boufi, S., González, I., Delgado-Aguilar, M., Tarrès, Q., Pèlach, M.À., and Mutjé, P. (2016). Nanofibrillated cellulose as an additive in papermaking process: a review. Carbohydr. Polym. *154*, 151–166.

48. Filatov, M.A., Baluschev, S., and Landfester, K. (2016). Protection of densely populated excited triplet state ensembles against deactivation by molecular oxygen. Chem. Soc. Rev. *45*, 4668–4689.

49. Zheng, D.-J., Yang, Y.-S., and Zhu, H.-L. (2019). Recent progress in the development of small-molecule fluorescent probes for the detection of hydrogen peroxide. Trends Analyt. Chem. *118*, 625–651.

50. Frisch, M., Trucks, G., Schlegel, H., Scuseria, G., Robb, M., Cheeseman, J., Scalmani, G., Barone, V., Petersson, G., and Nakatsuji, H. (2016). Gaussian 16 (Gaussian, Inc.).

51. Beck, A.D. (1993). Density-functional thermochemistry. III. The role of exact exchange. J. Chem. Phys. *98*, 5648–5656.

52. Parr, R.G. (1980). Density functional theory of atoms and molecules. In Horizons of quantum chemistry (Springer), pp. 5–15.

53. Lee, C., Yang, W., and Parr, R.G. (1988). Development of the Colle-Salvetti correlation-energy formula into a functional of the electron density. Phys. Rev. B. *37*, 785.

54. Andrew, R.L. (2001). Molecular Modeling Principles and Applications (Prentice Hall).

55. Yan, D., Lu, J., Wei, M., Li, H., Ma, J., Li, F., Evans, D.G., and Duan, X. (2008). In situ polymerization of the 4-vinylbenzenesulfonic anion in Ni-Al-layered double hydroxide and its molecular dynamic simulation. J. Phys. Chem. A. *112*, 7671–7681.

56. Rappe, A.K., and Goddard, W.A., III (1991). Charge equilibration for molecular dynamics simulations. J. Phys. Chem. *95*, 3358–3363.

57. Maple, J.R., Hwang, M.J., Stockfisch, T.P., Dinur, U., Waldman, M., Ewig, C.S., and Hagler, A.T. (1994). Derivation of class II force fields. I. Methodology and quantum force field for the alkyl functional group and alkane molecules. J. Comput. Chem. *15*, 162–182.

58. Andersen, H.C. (1980). Molecular dynamics simulations at constant pressure and/or temperature. J. Chem. Phys. *72*, 2384–2393.

59. Berendsen, H., Postma, J., Van Gunsteren, W., Hermans, J. (1981). In Intermolecular forces 331–342. Dordrecht: R.B. Pullman, ed.

60. Module, D. (2003). MS Modeling, Version 2.2 (Accelrys Inc.).